Ab Initio Study of Sodium Insertion in the λ-Mn_2O_4 and Dis/Ordered λ-$Mn_{1.5}Ni_{0.5}O_4$ Spinels

Vasileiadis, Alexandros; Carlsen, Brian; De Klerk, Niek J.J.; Wagemaker, Marnix

DOI
10.1021/acs.chemmater.8b01634

Publication date
2018

Document Version
Final published version

Published in
Chemistry of Materials

CHEMISTRY OF MATERIALS
Cite This: Chem. Mater. 2018, 30, 6646−6659
Article
pubs.acs.org/cm

Ab Initio Study of Sodium Insertion in the λ-Mn_2O_4 and Dis/Ordered λ-$Mn_{1.5}Ni_{0.5}O_4$ Spinels

Alexandros Vasileiadis,[†] Brian Carlsen,[†] Niek J. J. de Klerk,[†] and Marnix Wagemaker*[,†]

[†]Storage of Electrochemical Energy (SEE), Department of Radiation Science and Technology, Faculty of Applied Sciences, Delft University of Technology, Mekelweg 15, 2629 JB Delft, The Netherlands

Supporting Information

ABSTRACT: The main challenge of sodium-ion batteries is cycling stability, which is usually compromised due to strain induced by sodium insertion. Reliable high-voltage cathode materials are needed to compensate the generally lower operating voltages of Na-ion batteries compared to Li-ion ones. Herein, density functional theory (DFT) computations were used to evaluate the thermodynamic, structural, and kinetic properties of the high voltage λ-Mn_2O_4 and λ-$Mn_{1.5}Ni_{0.5}O_4$ spinel structures as cathode materials for sodium-ion batteries. Determination of the enthalpies of formation reveal the reaction mechanisms (phase separation vs solid solution) during sodiation, while structural analysis underlines the importance of minimizing strain to retain the metastable sodiated phases. For the λ-$Mn_{1.5}Ni_{0.5}O_4$ spinel, a thorough examination of the Mn/Ni cation distribution (dis/ordered variants) was performed. The exact sodiation mechanism was found to be dependent on the transition metal ordering in a similar fashion to the insertion behavior observed in the Li-ion system. The preferred reaction mechanism for the perfectly ordered spinel is phase separation throughout the sodiation range, while in the disordered spinel, the phase separation terminates in the $0.625 < x < 0.875$ concentration range and is followed by a solid solution insertion reaction. Na-ion diffusion in the spinel lattice was studied using DFT as well. Energy barriers of 0.3−0.4 eV were predicted for the pure spinel, comparing extremely well with the ones for the Li-ion and being significantly better than the barriers reported for multivalent ions. Additionally, Na-ion macroscopic diffusion through the 8a-16c-8a 3D network was demonstrated via molecular dynamics (MD) simulations. For the λ-$Mn_{1.5}Ni_{0.5}O_4$, MD simulations at 600 K bring forward a normal to inverse spinel half-transformation, common for spinels at high temperatures, showing the contrast in Na-ion diffusion between the normal and inverse lattice. The observed Ni migration to the tetrahedral sites at room temperature MD simulations explains the kinetic limitations experienced experimentally. Therefore, this work provides a detailed understanding of the (de)sodiation mechanisms of high voltage λ-Mn_2O_4 and λ-$Mn_{1.5}Ni_{0.5}O_4$ spinel structures, which are of potential interest as cathode materials for sodium-ion batteries.

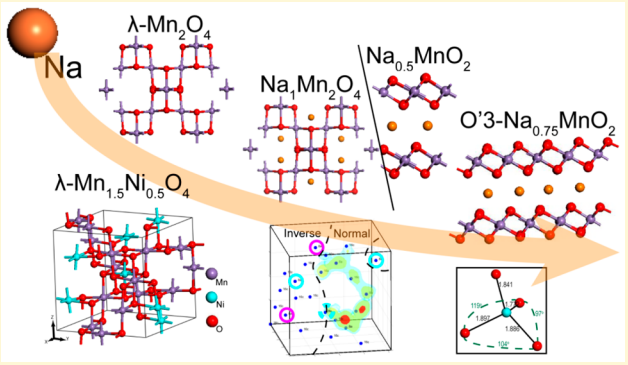

1. INTRODUCTION

Conventional power sources are being rapidly replaced by renewable power sources as demanded for a sustainable energy future. Successful implementation of these renewable power sources would benefit from large scale electrochemical storage, both to lift the intermittency in power generation and to provide grid stabilization.[1] For this application, state-of-the-art Li-ion batteries are anticipated to be costly; therefore, scientific interest has been directed toward alternative, cost-effective, and environmentally benign battery chemistries.[2,3]

Sodium ion and sodium aqueous batteries (SIBs, SABs) have been extensively studied in the past decade.[4,5] Utilizing Na-ion as a charge carrier ensures abundance and availability compared to its Li-ion counterpart.[6] Furthermore, the replacement of organic electrolytes with water in SABs provides a reduction in production cost and increases safety by practically eliminating the flammability of the system.[7] These batteries, however, do have their own challenges. The larger Na ionic radius, as compared to the Li ionic radius, often causes greater lattice distortions, which may compromise cycle life.[8] In addition, for an aqueous system, the dissociation potential of water restricts the battery voltage and thereby the amount of candidate electrode materials and limits the maximum power and energy density.[7,9] However, for stationary storage, gravimetric and volumetric energy, and power density, demands are less stringent. For the commercialization of large-scale battery applications, the primary criteria are cost-effectiveness, stability, and environmental friendliness, for which sodium aqueous systems appear to be promising candidates.[4,7]

Extensive research over the last five years has produced a large variety of electrode materials for sodium-ion battery

Received: April 19, 2018
Revised: September 11, 2018
Published: September 13, 2018

systems, with phosphate- and oxide-based structures dominating the scene.[4] Among them, the manganese oxide family stands out, offering many different structures suitable for Na-ion insertion, such as the layered P2-, P3-, and O3-type structures and the spinel structures.[10−13] In this study, we focused on the delithiated λ-Mn_2O_4 and λ-$Mn_{1.5}Ni_{0.5}O_4$ (λ-MNO) spinels, the lattice of which offers tetrahedral (8a) and octahedral (16c) interstitial positions, capable of Na insertion, along with a 3D Na-ion diffusion network.

Initial electrochemical sodiation of the pure spinel (λ-Mn_2O_4) has been shown to cause a partial phase transition from the spinel to the O′3 layered structure, caused by lattice deformations induced by Na insertion,[14,15] thus questioning the stability of the λ-$Na_1Mn_2O_4$ structure. On the other hand, more recent experiments suggest that reversible Na-ion (de)insertion into the spinel framework is possible by initially filling the 8a tetrahedral sites and then the remaining 16c octahedral sites.[16,17] Taking advantage of the stability in aqueous electrolytes, λ-Mn_2O_4 has been successfully implemented in SABs systems, showing high capacities and rate capabilities and stable cycling behavior at neutral pH.[16,17] Furthermore, the cost-effectiveness of SABs of λ-Mn_2O_4 spinel structure has been demonstrated.[16] In addition to Na, the pure spinel is also interesting in the context of its ability to store multivalent charge carriers such as Ca, Al, Zn, and Mg, as shown both experimentally[18] and computationally.[19] Based on the smaller ionic radii of Zn and Mg compared to that of Na, these charge carriers are expected to be more easily inserted.[18]

The λ-MNO spinel can be indexed by the $P4_332$ space group if Ni is ordered on the metal sublattice or by the $Fd\bar{3}m$ space group if Mn and Ni are randomly distributed on the metal sublattice.[20−25] The Ni distribution, and thus the resulting symmetry, strongly depends on the synthesis route of the lithiated counterpart (λ-LMNO), from which the delithiated host is obtained via electrochemical or chemical Li deinsertion.[10,11,21,24,25] Sodiation of the ordered and disordered λ-MNO spinels was recently studied by Kim and colleagues, who reported reversible Na (de)insertion in the tetrahedral (8a) interstitial sites of the spinel lattice.[10,11] A flat voltage plateau in the region of 3.65 V vs Na/Na^+ is reported, which is 0.56 V higher than in the pure spinel,[10] followed by a sharp voltage decline toward the λ-$Na_1Mn_{1.5}Ni_{0.5}O_4$ phase.[10,11] Both the ordered and the disordered phase display mixed phase separation and solid solution reaction pathways, the concentration ranges of which appear to depend on the cycling conditions.[10,11] Similar to Li-ion batteries,[20,25] the disordered phase exhibits better electrochemical performance, even though both the ordered and disordered structures have similar Li-ion diffusion coefficients.[11] Considerable kinetic barriers which hinder complete desodiation are reported, and nanosizing is suggested to achieve good performance.[10,11]

Herein, a thorough ab initio study of the thermodynamic and kinetic properties of the Na-ion insertion of λ-Mn_2O_4 and the various phases of the λ-$Mn_{1.5}Ni_{0.5}O_4$ (λ-MNO) spinels is presented. Detailed structural and thermodynamic analysis throughout the sodiation process aims to clarify key experimental observations regarding phase stability and reaction mechanisms. The Mn/Ni distribution in the λ-MNO lattice is shown to determine the sodiation reaction mechanism, in a fashion that closely resembles the behavior observed in Li-ion batteries.[26,27] In combination with a detailed investigation of Na-ion diffusion mechanics, a comprehensive picture of the fundamental processes is brought forward, in the context of which experimental optimization criteria[11] are addressed.

2. METHODS

Spin-polarized density functional theory (DFT) calculations were performed using the Vienna Ab Initio Simulation Package (VASP).[28] The PBE exchange correlation functional of Perdew and colleagues[29,30] was implemented, and valence-core interactions were probed with the projector-augmented wave approach (PAW).[31] The calculations were carried out with Hubbart U-corrections to correctly capture the behavior of heavily localized electronic ground states.[32,33] Effective $U-J$ parameters of U_{eff} = 3.9 and U_{eff} = 6.4 were used for Mn and Ni, respectively, based on previous DFT studies.[19,34−36] An energy cutoff energy of 520 eV and a 4 × 4 × 4 k-point mesh were selected to ensure accurate calculations, and total energies were obtained from successive self-consistent calculations.

Total energies of the ferromagnetic (FM) and various antiferromagnetic (AFM) configurations were calculated, with the FM solutions giving the lowest energy in both the λ-Mn_2O_4 and the λ-$Mn_{1.5}Ni_{0.5}O_4$. Therefore, all simulations were initialized with FM ordering. Although an AFM ordering has been experimentally reported,[37] according to the Goodenough−Kanamoru rule, an FM description might be appropriate considering the ridge sharing between oxygen octahedra.[38] For the lithiated λ-$Li_1Mn_{1.5}Ni_{0.5}O_4$ phase, both experiments and calculations reveal that AF ordering is more stable than FM ordering.[39,40] However, subtle differences in the calculated voltage profiles (0.03 V) are reported when comparing AFM and FM descriptions.[39] For simplicity, in this study, we retain the FM description throughout the computations.

The thermodynamic stability of the Na-insertion systems was determined by calculating the enthalpies of formation (H_f), according to eq 1:[41,42]

$$H_f = E_{Na_xHost} - xE_{Na_{x_{max}}Host} - (1-x)E_{Host} \quad (1)$$

where H_f represents the relative stability of a particular configuration, E_{Na_xHost} is the total crystal energy of the particular configuration, with x fractional sodium concentration, $E_{Na_{x_{max}}Host}$ the energy of the fully sodiated structure, and E_{Host} the energy of the empty host. The average sodium-insertion equilibrium voltage can be derived based on the difference in the Gibbs free energy between the sodiated and desodiated phases:

$$\bar{V} = \frac{-[E_{Na_xHost} - (x-y)E_{Na_s} - E_{Na_yHost}]}{(x-y)e} \quad (2)$$

This difference can be linked to the total energy change of the system throughout the sodiation process, according to eq 2,[43,44] where E_{Na_xHost} and E_{Na_yHost} are the total energies of the Na_xHost and Na_yHost configurations, respectively. E_{Na_s} is the sodium energy, and e is the electron charge.

Na diffusion was studied with the nudge elastic band (NEB) method, utilizing the climbing image approach and molecular dynamics (MD) simulations. For the dilute vacancy limit of the pure spinel, the 8a-16c energy path was converged and symmetrically replicated to create an 8a-16c-8a path. To ensure viable computational times for the MD simulations, the energy cutoff energy and the k-point sampling were reduced to 400 eV and 1 × 1 × 1, respectively. The total simulation time was between 0.25 and 0.5 ns at a constant temperature of 600 and 300 K. Each time-step was set to 2 fs, and the first 2.5 ps were discarded as equilibration time. Analysis of the MD simulations was done according to the approach reported recently.[45] In one of the MD simulations (600 K) of the λ-Mn_2O_4 spinel, the lattice broke down to a collection of particles after 0.45 ns. As will be discussed herein, this may be due to the metastability of the spinel phase. Analysis was performed only for the time frame where the spinel framework remained intact. Proper determination of activation energies and diffusion coefficients via MD calculations would require more and longer MD simulations at higher temperatures in larger

DOI: 10.1021/acs.chemmater.8b01634
Chem. Mater. 2018, 30, 6646−6659

supercells. For this reason, we refrain from presenting a quantitative behavior and use the MD picture as an insightful qualitative tool.

The optimized unit cells of the λ-Mn_2O_4 and $Mn_{1.5}Ni_{0.5}O_4$ crystal structures contain 48 atoms ($Mn_{16}O_{32}$, $Mn_{12}Ni_4O_{32}$). The 8 formula units provide 16 sodium insertion steps to reach a 1 to 1 ratio between the transition metals and sodium. For the disordered λ-(Li)$Mn_{1.5}Ni_{0.5}O_4$ phase, a slight stoichiometric excess of Mn,[10,20] oxygen deficiencies,[23,25,46] or partial fluorine replacement[10] have been reported. For the purposes of this study, the stoichiometry was kept constant to the standard ratio of one Ni for every three Mn atoms. The selection of the representative λ-$Mn_{1.5}Ni_{0.5}O_4$ hosts was based on the relaxation and energy minimization of inequivalent configurations, differing in the Ni/Mn distribution in both the lithiated and empty spinel, and is thoroughly discussed in the next section.

3. RESULTS

3.1. λ-Mn_2O_4 and λ-$Mn_{1.5}Ni_{0.5}O_4$ Host Structures. The structure of λ-Mn_2O_4 spinel was relaxed, starting from the experimentally determined structure.[47] The relaxed λ-Mn_2O_4 configuration represents the cubic $Fd\bar{3}m$ unit cell shown in Figure 1. The spinel structure offers two types of interstitial sites: the tetrahedral (8a) and the octahedral (16c).

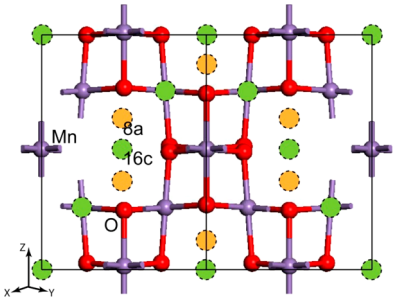

Figure 1. Unit cell of the pure λ-Mn_2O_4 spinel: orange and green circles indicate the interstitial tetrahedral (8a) and octahedral (16c) sites, respectively. Red and purple spheres represent O and Mn atoms, respectively.

Experimentally, the most common way of obtaining the empty spinel structures (λ-Mn_2O_4, λ-$Mn_{1.5}Ni_{0.5}O_4$) is by synthesizing the lithiated phases ($LiMn_2O_4$, $LiMn_{1.5}Ni_{0.5}O_4$), where lithium occupies the tetrahedral interstitial position. Either with chemical[14,17] or electrochemical[10,14] delithiation, lithium is removed from the lattice, thus leaving vacant tetrahedral sites for subsequent sodium insertion. This implies that the empty host configurations will be determined by the lithiated host structures and thus are relevant to investigate. Where the pure spinel is indexed by the $Fd\bar{3}m$ space group, the symmetry of the Ni doped $LiMn_{1.5}Ni_{0.5}O_4$ spinel depends on the cation distribution. Depending on the synthesis route,[21,24,25] the result is either a faced-centered cubic spinel lattice (space group $Fd\bar{3}m$), when Ni and Mn randomly occupy the transition metal sublattice, or a lower-symmetry cubic primitive spinel lattice (space group $P4_332$), when Ni and Mn are ordered on the transition metal sublattice.[20−25]

Prior to the selection of the $Mn_{1.5}Ni_{0.5}O_4$ host structures, total crystal energies of all the inequivalent Mn/Ni configurations of both the fully lithiated ($Li_1Mn_{1.5}Ni_{0.5}O_4$) and delithiated ($Mn_{1.5}Ni_{0.5}O_4$) phases of the $Fd\bar{3}m$ lattice in one unit cell were determined. The total energies provide a thermodynamic argument on the selection of the $Mn_{1.5}Ni_{0.5}O_4$ host structures. We chose to examine the lithiated phases ($Li_1Mn_{1.5}Ni_{0.5}O_4$) as well because of the preparation method. As it was discussed in the previous paragraph, host structures cannot be prepared directly in the sodiated form ($Na_1Mn_{1.5}Ni_{0.5}O_4$), but come from the delithiated spinels. However, this link holds true assuming that the host framework remains unchanged upon cycling, keeping the same Ni distribution. As we will unravel in a later stage of this paper, Ni is mobile in the host framework, and thus, there is a possibility of Ni rearrangement, leading to interconversion between the various configurations.

The lowest energy configuration of the fully lithiated phase exhibits Ni ordering in the transition metal sites, resulting in the $P4_332$ symmetry. This is in agreement with previous DFT results[26] and experimental studies, which suggest that the disordered phase appears at higher annealing temperatures,[25] thus indicating that the ordered structure is the most stable configuration of $Li_1Mn_{1.5}Ni_{0.5}O_4$. The ordered structure (Figure 2a) was selected for the present computational

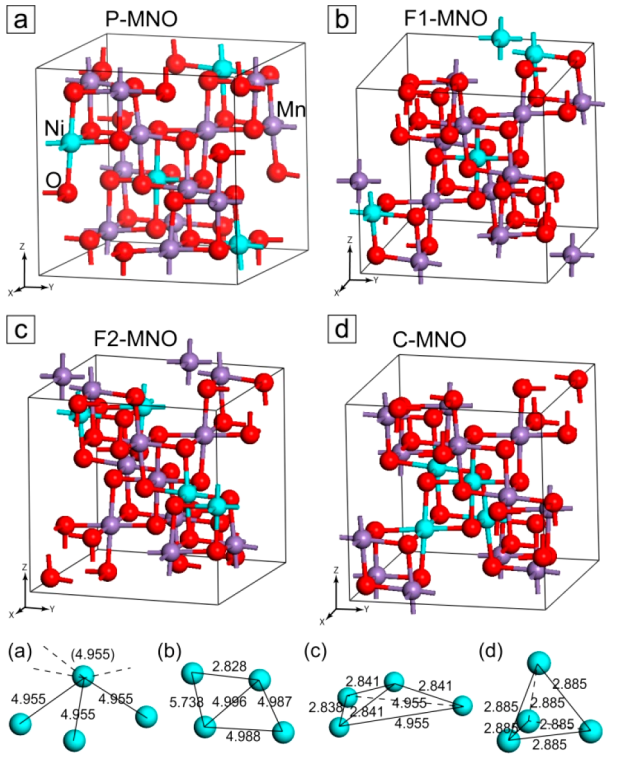

Figure 2. Unit cells of the (a) ordered P−$Mn_{1.5}Ni_{0.5}O_4$ configuration, (b) disordered F1−$Mn_{1.5}Ni_{0.5}O_4$ configuration, (c) disordered F2−$Mn_{1.5}Ni_{0.5}O_4$ configuration, and (d) C−$Mn_{1.5}Ni_{0.5}O_4$ configuration, exhibiting Ni clustering. Below, the relative Ni position within one unit cell is presented.

study, and it is referred to as P−$Mn_{1.5}Ni_{0.5}O_4$, named after the initial letter of its symmetry. Additionally, the lowest energy disordered configuration (second lowest overall) having a random distribution of Ni in the spinel lattice ($Fd\bar{3}m$) was selected and is shown in Figure 2b. We refer to the disordered variant as F1−$Mn_{1.5}Ni_{0.5}O_4$, as it will represent the disordered variant described by the $Fd\bar{3}m$ lattice.

When investigating all the inequivalent $Mn_{1.5}Ni_{0.5}O_4$ configurations, however, the lowest energy configuration exhibits Ni clustering in side-sharing octahedra (Figure 2d). The relative Ni position in the lattice forms a tetrahedron with a Ni−Ni distance of 2.887 Å. This is the smallest Ni−Ni distance possible, resulting in segregation of the Ni and Mn

DOI: 10.1021/acs.chemmater.8b01634
Chem. Mater. 2018, 30, 6646−6659

atoms. Ni clustering within the unit cell can be regarded as a different ordered state, where the symmetry results in the $P\bar{4}3m$ space group, with Ni occupying the 4e position. This Ni configuration is often regarded as unrealistic,[26,27] and it is in fact the highest energy structure according to our calculations when minimizing all the $Li_1Mn_{1.5}Ni_{0.5}O_4$ inequivalent configurations. Nonetheless, it may be a relevant configuration under delithiated or desodiated (charged) conditions and was studied as an extreme opposite case to the ordered structure. We refer to this configuration as C−$Mn_{1.5}Ni_{0.5}O_4$ structure, with the letter C referring to the word "clustered". Another $Mn_{1.5}Ni_{0.5}O_4$ configuration with high Ni clustering is presented in Figure 2c. This structure was studied as another disordered representative ($Fd\bar{3}m$), referenced as F2−$Mn_{1.5}Ni_{0.5}O_4$. In this case, the four nickel atoms form a tetrahedron with vertices in adjacent sites. The tetrahedron has an isosceles triangle as a base with one side 2.84 Å and the other two 4.93 Å long, creating angles of 35.3 and 73.4°, respectively. Because Ni can occupy discrete transition metal sites in the spinel lattice, Ni placement in F2−MNO is the second most clustered distribution.

A qualitative trend observed by the minimization of the inequivalent spinel variants ($Mn_{1.5}Ni_{0.5}O_4$, $Li_1Mn_{1.5}Ni_{0.5}O_4$) is that the fully lithiated spinels are stabilized by having the Ni atoms well distributed, whereas the empty spinels are stabilized by the formation of Ni clusters. However, the relative stability of the two configurations is quite different. In the $Li_1Mn_{1.5}Ni_{0.5}O_4$ case, there is a clear energy preference for the ordered phase (Figure 3). On the other hand, in the empty host case, the energies of all configurations lie within a range of only 25 meV per unit cell.

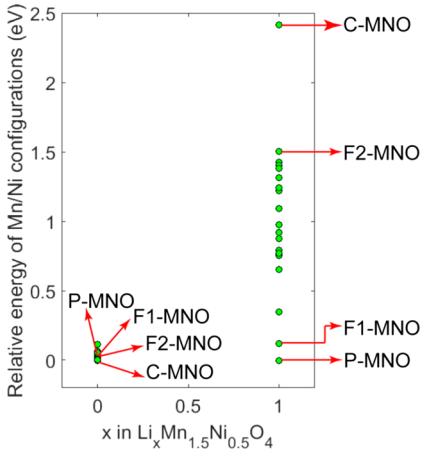

Figure 3. Mn/Ni inequivalent energy configurations in the empty and filled unit cell structures.

This indicates that a direct synthesis of the empty spinel, if possible, will not lead to the C−$Mn_{1.5}Ni_{0.5}O_4$ or F2−$Mn_{1.5}Ni_{0.5}O_4$ structures. The mixing entropy in room temperature would favor a truly disordered phase, where Mn and Ni randomly occupy the octahedral sites. In addition, a direct synthesis process seems difficult, as shown by Kitchaev and colleagues.[48]

The lattice parameters of all relevant structures mentioned above are compared with experimental values in Table 1. For all structures, the lattice parameters are in good agreement with the experimental ones, showing differences of 2.5%, which is a typical overestimation when utilizing the Hubbart correction method.[26,49−51] Small differences are observed between the λ-MNO variants, with the ordered structure having the smallest lattice parameters, which is in agreement with a previous experiment.[25]

Table 1. Comparison between Experimental and Simulated Lattice Parameters

λ-Mn_2O_4	a (Å)
DFT	8.242
experimental[47]	8.064
λ-$Mn_{1.5}Ni_{0.5}O_4$	a (Å)
(P) DFT	8.142
(P) experimental[25]	8.005
(F1) DFT	8.159
(F2) DFT	8.163
(C) DFT	8.162

3.2. Structure and Thermodynamics upon Na-Ion Insertion. *3.2.1. Na-Ion Insertion in λ-Mn_2O_4.* The convex hull (Figure 4a) obtained for Na insertion into λ-Mn_2O_4 indicates that sodiation initially occurs via a two-phase separation from the empty spinel phase toward the $Na_1Mn_2O_4$ phase. During this first-order phase transition, inserted Na-ions are accommodated on the tetrahedral 8a positions, which provides a considerably lower energy environment (>165 meV), compared to the octahedral 16c positions. This is followed by a subsequent phase separation transition from $Na_1Mn_2O_4$ toward $Na_2Mn_2O_4$, during which the additional Na-ions are accommodated by the octahedral 16c sites. At the same time, the Na-ions in the 8a sites migrate to the remaining 16c sites. The predicted phase separation mechanisms suggest that, at 0 K, the sodiation process can be described by eqs 3 and 4:

$$()_{8a}[]_{16c}[Mn_2]_{16d}[O_4]_{32e} \rightarrow (Na_1)_{8a}[]_{16c}[Mn_2]_{16d}[O_4]_{32e} \quad (3)$$

$$(Na_1)_{8a}[]_{16c}[Mn_2]_{16d}[O_4]_{32e} \rightarrow ()_{8a}[Na_2]_{16c}[Mn_2]_{16d}[O_4]_{32e} \quad (4)$$

This is in agreement with the more general proposed insertion equations[17] 5 and 6.

$$()_{8a}[]_{16c}[Mn_2]_{16d}[O_4]_{32e} \rightarrow (Na_x)_{8a}[]_{16c}[Mn_2]_{16d}[O_4]_{32e} \quad (5)$$

$$(Na_x)_{8a}[]_{16c}[Mn_2]_{16d}[O_4]_{32e} \rightarrow (Na_x)_{8a}[Na_y]_{16c}[Mn_2]_{16d}[O_4]_{32e} \quad (6)$$

The large volume change of 16% upon formation of $Na_1Mn_2O_4$, which increases to 26% upon reaching the fully sodiated $Na_2Mn_2O_4$ phase, as shown in Figure 4b, suggests that mechanical stresses will cause mechanical degradation upon cycling. In addition, considering that the material is predicted to phase separate, the significant lattice mismatch between the end-member phases (Mn_2O_4, $Na_1Mn_2O_4$, $Na_2Mn_2O_4$) may lead to crack formation and mechanical failure upon cycling. Indeed, mechanical degradation has been reported experimentally[10,15,17] where XRD peak broadening was ascribed to lattice strain and partial amorphization of the structure upon Na-ion insertion.[15,17] Additionally, it has been observed[15] that Na insertion induces a partial phase transformation toward the layered O′3−Na_xMnO_2 lattice. In a previous study, it was shown that such transformations can be predicted by DFT calculations.[52] In that case, it was

DOI: 10.1021/acs.chemmater.8b01634
Chem. Mater. 2018, 30, 6646−6659

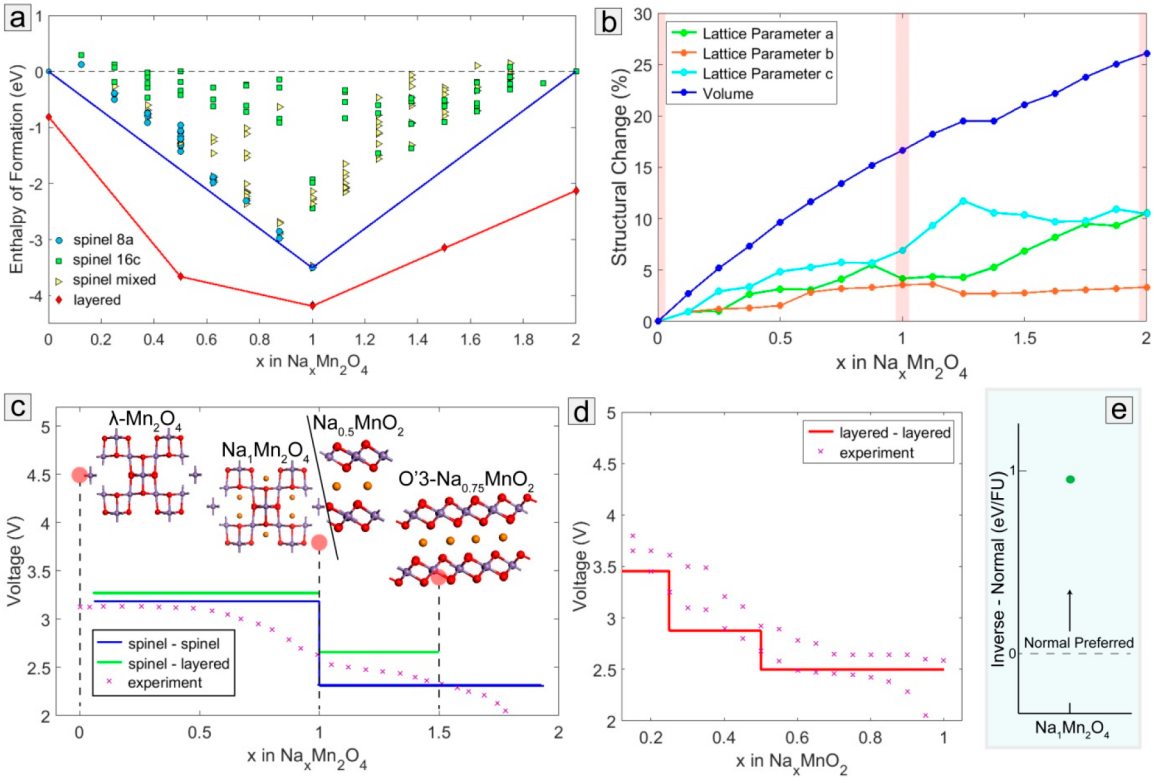

Figure 4. (a) Enthalpies of formation and convex hull of Na insertion in λ-Mn_2O_4 and layered O3 MnO_2. Cyan circles, green squares, and yellow triangles represent Na inserting into only 8a, only 16c, and mixed spinel interstitial sites, respectively. Red diamonds represent Na intercalation in the O3 layered structure. Blue and red lines follow the lowest enthalpy path of the spinel and layered structure, respectively. (b) Structural changes during Na insertion in λ-Mn_2O_4: the light red vertical lines indicate the stable phases during the sodiation process. (c) Calculated (blue line) vs experimental[10,15] (scatter) voltage profile of Na insertion in λ-Mn_2O_4. The experimental data were normalized according to what is considered as full capacity reaching the $Na_1Mn_2O_4$ and $Na_1Mn_{1.5}Ni_{0.25}O_4$ phase.[10,15] The green lines indicate the average voltages between the spinel and the layered O′3−$Na_{0.5}MnO_2$ and O′3−$Na_{0.75}MnO_2$ monoclinic phases (please note the different stoichiometric notation). (d) Calculated (red line) vs experimental[54] (scatter) voltage profile of Na intercalation in the layered O3 structure. (e) The relative stability of the normal vs inverse spinel for the $Na_1Mn_2O_4$ concentration, where FU is the $Na_1Mn_2O_4$ formula unit.

demonstrated that Na-ion insertion into the rutile tunnel of hollandite TiO_2 leads to a phase transformation toward the O′3 layered lattice. For Na-ion insertion in the spinel λ-Mn_2O_4 structure, however, such a transformation was not observed. This is in agreement with recent electrochemical tests in an aqueous environment, showing highly reversible (de)insertion behavior of Na-ions in λ-Mn_2O_4 and high rate capabilities.[16,17] Despite the strain, no new phases were observed, and the constant voltage (CV) peaks were ascribed to Na-ion insertion into 8a and 16c spinel sites.[16,17] The metastability, however, of the sodiated spinel phases is evident in literature.[48,53] Kitchaev and colleagues performed a thorough thermodynamic DFT study to investigate the phase selection upon synthesizing a variety of A_xMnO_2 polymorphs (α, β, γ, δ, λ, R) with A = Li^+, Na^+, Ca^{2+}, K^+, Mg^{2+}.[48] The spinel phase (λ) was found to be metastable compared to the layered O3 phase (δ) throughout the sodiation range due to the incompatibility of the spinel interstitial sites with the large Na-ions.[48] This indicates the presence of a driving force toward the layered structure. In this study, to evaluate a possible spinel to layered transition, the O3 layered $NaMnO_2$ phase was also optimized, starting from the experimental lattice.[54] By Na deintercalation, the lowest energy configurations of the monoclinic phases were determined. The O3-layered enthalpies of formation with respect the spinel end-member phases are presented in Figure 4a, revealing the relative stability of the MnO_2 structures. To evaluate the presence of a thermodynamic driving force behind the spinel-layered structure transformation, the average voltages between the spinel phases (λ-Mn_2O_4, $Na_1Mn_2O_4$) and the monoclinic layered phases (O′3−$Na_{0.75}MnO_2$, O′3−$Na_{0.5}MnO_2$) were determined and are presented in comparison with the calculated voltage profile while remaining in the spinel structure (λ-Mn_2O_4, $Na_1Mn_2O_4$, $Na_2Mn_2O_4$) in Figure 4c.

The two plateaus (blue lines) in Figure 4c reflect the two spinel−spinel phase separation mechanisms predicted, according to the convex hull (λ-Mn_2O_4 → $Na_1Mn_2O_4$ and $Na_1Mn_2O_4$ → $Na_2Mn_2O_4$). Our calculations indicate that the first reaction occurs at 3.2 V and the second at 2.3 V, in good agreement with experiments.[10,15] The slight slope in the experimental voltage profile might be the result of the large lattice mismatch during the phase transition, which usually leads to poor Na-ion kinetics over the phase interfaces and grain boundaries, inducing large overpotentials. An example of a similar voltage evolution behavior is the lithiation of anatase TiO_2. The phase transition between $Li_{0.5}TiO_2$ and $LiTiO_2$ shows a clear plateau during extremely slow cycling and/or for very small particle sizes, while during standard cycling conditions, a slope is seen due to kinetically induced overpotentials.[55] A thick phase interface layer is also linked with a large gradient penalty (κ), penalizing the coexistence of two phases.[56] Therefore, the inserted spinel system will be more susceptible to suppression of phase separation. Suppression of the phase separation

DOI: 10.1021/acs.chemmater.8b01634
Chem. Mater. 2018, 30, 6646−6659

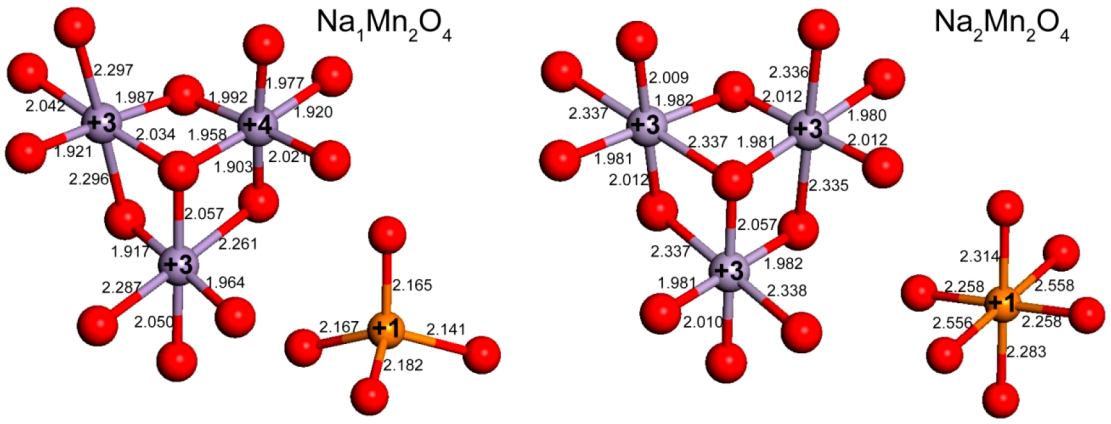

Figure 5. Local atomic environment and oxidation states of Mn octahedra and Na tetrahedra.

mechanism can be achieved either by high currents[57−60] or by reducing the particle size to the thickness of the phase interface layer,[55] as simulated and shown experimentally for LFP and anatase TiO_2 electrodes. Thus, given the correct conditions, partial mixing of the end-member phases (solid solution) might be possible, leading to a sloping voltage curve.

The average voltages between the empty spinel and the O′3−$Na_{0.5}MnO_2$ layered phase (3.28 eV) and the spinel $Na_1Mn_2O_4$ and the layered O′3−$Na_{0.75}MnO_2$ phase (2.65 V) (green lines in Figure 4c) appear higher compared to the voltages of the Mn_2O_4 to $Na_1Mn_2O_4$ (3.19 V) and $Na_1Mn_2O_4$ to $Na_2Mn_2O_4$ (2.3 V) spinel−spinel phase transition, respectively. This result rationalizes the experimental observation[15] of a partial phase transformation toward the layered structure as an alternative sodiation route. Such a phase transition would require a significant amount of time because of the substantial kinetic barriers that must be overcome; although, at high Na concentrations, it could be catalyzed by a gradual deformation of the spinel lattice due to strain. This is consistent with experiments showing that the partial formation of the layered phase appears after 10 cycles.[15] For completion, the calculated sodiation voltage profile of the layered structure is presented in Figure 4d, showing good agreement with experiments.[54]

The $Na_1Mn_2O_4$ spinel structure was found to be metastable in another DFT study[53] as well, this time compared to the post spinel CF−NMO phase. Herein, the CF−NMO structure was computationally optimized starting from the experimental lattice.[61] The $Na_1Mn_2O_4$ spinel phase is found to be metastable compared to both the layered and the CF phase, in agreement with previous results.[48,53] However, the CF phase appears only at higher pressures and temperatures[61] and thus only the comparison with the O3 phases is relevant to battery cycling.

Retaining the spinel framework intact would require steps for minimizing strain, which may be catalyzing unwanted transformations during Na insertion. Suppression of the phase separation, as discussed above, is a good example. High rate cycling might be beneficial, not only by suppressing the first order phase transition but also simply by not providing sufficient time for the sluggish undesired phase transformations to occur. Nanosizing may be beneficial within this context, potentially suppressing phase separation and lowering strain, although surfaces may also be the starting point toward undesired phase transitions.

Another important consideration when implementing spinel structures is cation disorder leading to the conversion from a normal to an inverse spinel lattice. In the normal spinel of AB_2O_4 stoichiometry, A cations (in our case Na and/or vacancies) occupy the tetrahedral interstitial sites, and B (in our case Mn and/or Ni when studying MNO) occupy the octahedral spinel sites. In the inverse spinel, B occupy all the tetrahedral and half the octahedral sites, while A occupy the remaining octahedral sites.[62] Conversion to the inverse spinel structure under extreme conditions is a well-known problem creating kinetic limitations in the electrode.[19,63] Bhattacharya and colleagues methodically studied the normal vs inverse spinel stability for Li-ion batteries of various spinel oxides at 0 K, including (de)lithiated Mn_2O_4.[62] With regard to the lithiated phase, the normal spinel is reported to be thermodynamically much more favorable (∼1 eV/$Li_1Mn_2O_4$).[62] Here, similar to its Li counterpart, the normal spinel is found to be much more stable (0.97 eV/$Na_1Mn_2O_4$) compared to the inverse spinel of $Na_1Mn_2O_4$ stoichiometry, as shown in Figure 4e. Additionally, it should be noted that with regard to the delithiated Mn_2O_4 phase, the normal spinel is reported as only 23 meV lower in energy than the inverse spinel, raising concerns on the stability of the delithiated/desodiated state.[62]

All Mn−O bonds in the empty host (λ-Mn_2O_4) are close to an average value of 1.944 Å, which is slightly higher compared to a previous DFT study, which cited 1.914 Å and the experimentally determined value of 1.910 Å.[64] The $Na_1Mn_2O_4$ phase retains the spinel framework, although the symmetry is reduced due to Jahn−Teller (JT) distortions, a commonly observed phenomenon in octahedral transition metal complexes.[50,51,64,65] In the $Na_1Mn_2O_4$ phase, the insertion of Na, which donates its electron to the spinel lattice, reduces half of the Mn^{4+} to Mn^{3+}. The Mn^{3+} octahedra exhibit an elongation of two of the Mn−O bonds, as depicted in Figure 5, which illustrates the local atomic structures and oxidation states of the Mn octahedra for the stable end-member phases. The two longer Mn−O bonds of the Mn^{3+} octahedra have an average value of 2.285 Å, while the other bonds have an average value of 1.950 Å. With regard to the Mn^{4+} octahedra, all Mn−O bonds show an average value of 1.980 Å. This result causes changes in the unit cell parameters, increasing the *c*-axis by 0.28 Å compared to the *b*-axis, while the latter becomes 0.13 Å longer than the *a* lattice parameter; see Figure 4b and Table 2. Compared to the lithiated spinel,[64] the sodiated system shows a 65% larger distortion due to the larger ionic radius of the Na-

DOI: 10.1021/acs.chemmater.8b01634
Chem. Mater. 2018, 30, 6646−6659

Table 2. Lattice Parameters of the End Member Phases

	a (Å)	b (Å)	c (Å)	Mn oxidation state
Mn_2O_4	8.242	8.242	8.242	4+
$Na_1Mn_2O_4$	8.686	8.535	8.813	3+/4+
$Na_2Mn_2O_4$	9.110	8.517	9.106	3+

ions. It is important to acknowledge that the presented Jahn−Teller distortions are not unique. There is an infinite number of orderings that satisfy the bond length criteria explored within.[66] To obtain the lowest energy orderings (zigzag or collinear depending on the system), a full investigation according to the work of Radin et al. is required.[66]

The computations reproduce the cubic to tetragonal (I41/amd) lattice[10,15] transformation when Na is inserted to the 16c sites to form the $Na_2Mn_2O_4$ composition, similar to the Li analogue.[67] Only Mn^{3+} is present in this composition, and as a result, the a and c lattice constants become equal again due to alternating elongations in the respective octahedra (Figure 5).

3.2.2. Na-Ion Insertion in λ-$Mn_{1.5}Ni_{0.5}O_4$ and Mn/Ni Ordering: Reaction Mechanisms Dependence. Experimentally, Na-ion insertion in MNO spinel structures occurs up to a maximum composition of λ-$Na_1Mn_{1.5}Ni_{0.5}O_4$, where the Na ions occupy the tetrahedral 8a sites.[10,11] For this reason, DFT simulations were performed within this concentration range. In agreement with experimental observations, the present simulations resulted in a Na-ion occupancy of the tetrahedral 8a sites in the case of λ-$Na_1Mn_{1.5}Ni_{0.5}O_4$ composition.

Enthalpies of formation of the P, F1, F2, and C−MNO structures were determined as a function of Na content. The convex hull, the tie line that connects the lowest energy configurations, is shown for each of the MNO phases in Figure 6a. Interestingly, significantly different sodiation mechanisms are predicted for the four MNO phases.

The ordered structure (P−MNO) exhibits unstable intermediate phases during sodiation, except for two of the $Na_{0.5}Mn_{1.5}Ni_{0.5}O_4$ configurations, which are more stable by 52 meV, compared to the reference phases. Thus, the perfectly ordered material is expected to exhibit two first order phase transitions between $0 < x < 0.5$ and between $0.5 < x < 1$. Considering that the enthalpy of formation of the $Na_{0.5}Mn_{1.5}Ni_{0.5}O_4$ configuration is comparable to the thermal energy associated with room temperature (25 meV), in practice, one first order phase transition between the end-member phases may be observed.

For the disordered phases (F1 and F2−MNO), a notable shift in the stability of the intermediate configurations is predicted. At large sodium compositions, several configurations are predicted to be thermodynamically stable. Consequently, the disordered structure is expected to follow a two-phase reaction between $0 < x < 0.875$ and $0 < x < 0.625$ in the case of F1 and F2−MNO, respectively, followed by a solid solution reaction toward the $Na_1Mn_{1.5}Ni_{0.5}O_4$ composition. A phase separation region that terminates at $x = 0.75$ might also occur for both the disordered spinels because the convex line of the F1 and F2 variants is within 30 meV of $Na_{0.75}Mn_{1.5}Ni_{0.5}O_4$ and $Na_{0.625}Mn_{1.5}Ni_{0.5}O_4$, respectively. Regarding the C−MNO lattice, configurations at lower sodium concentrations fall on the convex hull, resulting in a much smaller two-phase region between $0 < x < 0.375$, where further sodiation is predicted to follow a solid solution reaction.

The enthalpies of formation allows us to predict the voltages, at 0 K, as shown in Figure 6b. The ordered phase

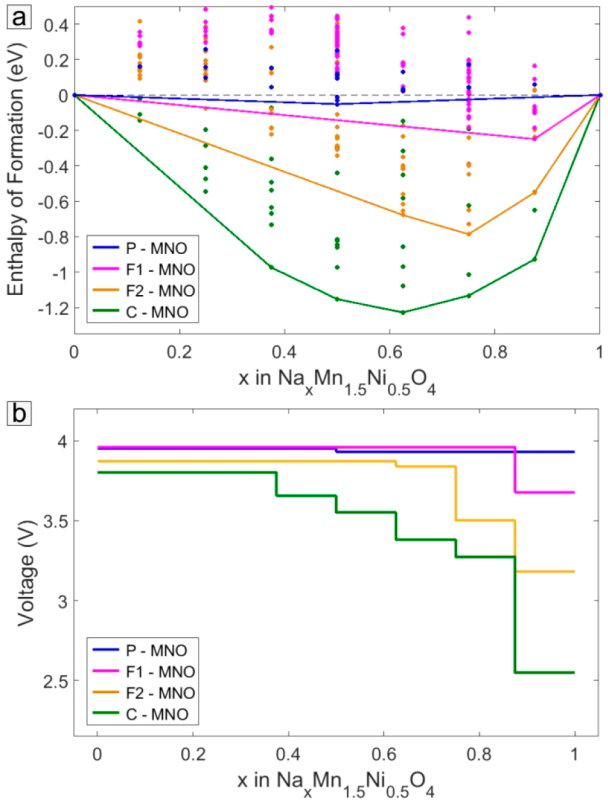

Figure 6. P, F1, F2, and C−MNO structures: (a) enthalpies of formation and convex hulls of Na-ion insertion and (b) voltage profiles.

(P−MNO) exhibits two voltage plateaus, reflecting the two-phase transitions. For the F1, F2, and C−MNO spinels, however, the voltage plateau, and thus the two-phase region, terminates before reaching the $Na_1Mn_{1.5}Ni_{0.5}O_4$ endmember composition, and it is followed by a potential drop via several compositions, indicating a solid solution mechanism. The two voltage plateaus of the P−MNO structure are very similar in voltage, a direct consequence of the marginal stability difference of the lowest energy $Na_{0.5}Mn_{1.5}Ni_{0.5}O_4$ compared to the endmember phases. The same holds for the two first voltage plateaus of the disordered F2−MNO structure, as observed in Figure 6b.

To better demonstrate the relative stability of the P, F1, F2, and C−MNO structures throughout the sodiation range, the enthalpy of formation figure was redrawn (Figure 7a) with respect to the P−MNO structure. Referring all MNO to the P−MNO configuration will not only enable a direct comparison of the relative stability at a given composition but also will additionally explain the effect of ordering on the energy environment of the structure during sodiation. Furthermore, in the latter section of this paper, we show Ni migrating from its original position in the host lattice. Considering that Ni is mobile in the host structure, the relative stability plot can reveal the driving forces that might lead to interconversions between the various configurations during sodiation. For example, the disordered F1−MNO variant is more stable than the P−MNO in the $0.75 < x < 0.875$ concentration region. Assuming interconversions are fully accessible within (de)sodiation time scales, both ordered and disordered structures are expected to phase separate up to the disordered F1−$Na_{0.875}Mn_{1.5}Ni_{0.5}O_4$ phase (Figure 7a).

DOI: 10.1021/acs.chemmater.8b01634
Chem. Mater. 2018, 30, 6646−6659

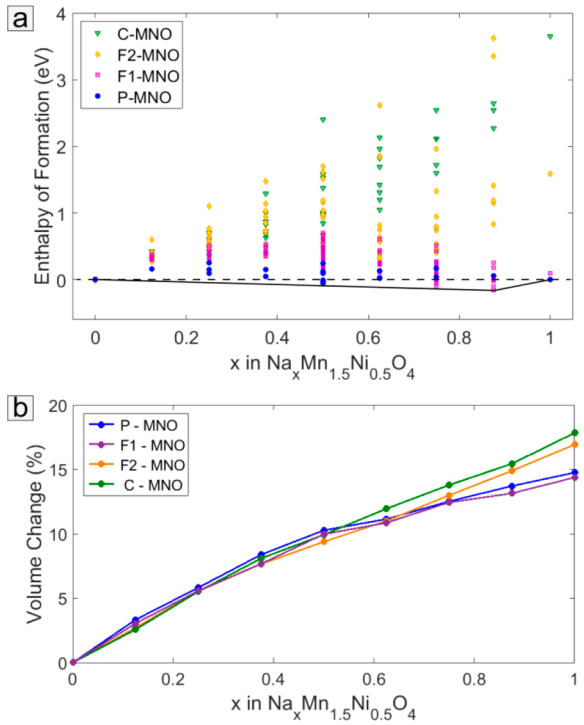

Figure 7. (a) Enthalpies of formation referenced to the P-MNO structure. (b) Volume changes for the MNO variants throughout the sodiation process.

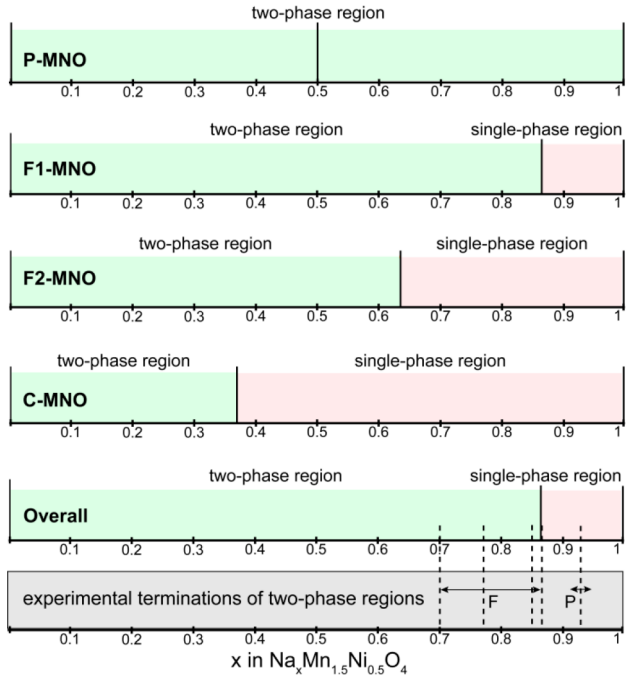

Figure 8. Reaction mechanisms of the P, F1, F2, and C−MNO structures during sodiation at 0 K. Solid vertical lines indicate the range of the two-phase separation (light green color) and single-phase regions (light red color). The overall thermodynamic profile refers to the lowest enthalpy path predicted when considering the relative stability of all configurations (Figure 7a). Below, the dashed lines indicate the experimentally determined[10,11] terminations of the two-phase region in both disordered (F) and ordered (P) structures.

Volume changes throughout the concentration range are presented in Figure 7b. Comparing the $Na_1Mn_{1.5}Ni_{0.5}O_4$ configurations, we observe that the F1 and P−MNO have the lowest volume change, followed by the Ni clustered variants F2 and C−MNO. The P−MNO displays the largest volume change; however, at the initial stages of sodiation, the structures with a more clustered Ni distribution appear to change less, as Na insertion occurs in the vicinity of the Ni cluster.

Kim and colleagues monitored the sodiation of both ordered (P) and disordered (F) MNO spinels ex situ, in situ, and in operando by X-ray diffraction, as well as with PITT and GITT measurements.[10,11] For the ordered phase the phase separation region was reported for a concentration range of $0 < x < 0.93$.[11] The disordered phase was shown to display a first order phase transition up to $x = 0.88$, followed by a solid solution toward the endmember $Na_1Mn_{1.5}Ni_{0.5}O_4$ phase.[11] Interestingly, the experimentally observed phase separation region varies depending on the experimental method, ending at $x = 0.70$, $x = 0.78$, $x = 0.87$, and $x = 0.88$ in $Na_xMn_{1.5}Ni_{0.5}O_4$, when measured at C/60 with X-ray,[10] C/40 with X-ray,[10] with GITT,[10] and GITT,[11] respectively. This was rationalized by the dynamic character of operando by X-ray diffraction, which affects the phase separation region, in contrast to the GITT measurements, which keep the system closer to thermodynamic equilibrium.[10] Subsequent Na (de)insertion in the ordered and disordered spinel structures was experimentally investigated as well.[11] A vast variety of two-phase regions and solid solution reaction mechanisms was reported, which appear to be different for the two structures but also appear to depend on the cycling conditions.[11]

The thermodynamic behavior at 0 K of the different spinel structures considered within, in comparison with experimental results,[10,11] is summarized in Figure 8. The simulations suggest that the Ni distribution through the spinel lattice alters the sodiation reaction mechanism, effectively modifying the extent of the phase separation region in good agreement with the experimental picture. The small differences in stability between the various configurations predicted at present may be easily bridged by the kinetically induced overpotentials or interconversion due to Ni rearrangement, rationalizing the diversity of reaction pathways observed experimentally. In addition, different preparation methods may result in different Ni distributions, which strongly influence the relative stability. However, we should be very critical when using Figure 8 to draw comparisons with experiments. Because the reaction mechanisms predicted herein refer to 0 K, the comparison presented has a speculative character. A complete phase stability study[27] is needed to estimate the temperature dependence at which the ordered states disorder, forming a solid solution. Gaining a more detailed insight would require Monte Carlo (MC) simulations of numerous configurations, similar to the approach followed by Lee et al.[27]

Also with regard to Li-ion insertion into λ-MNO, the impact of Mn/Ni ordering has been observed.[26,27] A favorable alternating pattern of lithium and vacancies in the spinel lattice was reported.[26] The uniform[27] disordered configuration was found to have a Mn/Ni arrangement that was compatible with this preferable Li/Va arrangement. Thus, the ground state of the disordered spinel was predicted to be the intermediate $Li_{0.5}Mn_{1.5}Ni_{0.5}O_4$ phase, explaining the origin of the small voltage step experimentally observed at this concentration.[26] Various two-phase regions were observed, up to a maximum composition of $0.5 < x < 1$, depending on the Mn/Ni ordering in LMNO variants, indicating the importance of the local Mn/

DOI: 10.1021/acs.chemmater.8b01634
Chem. Mater. 2018, 30, 6646−6659

Ni environment.[26] By utilization of grand canonical MC simulations, the phase diagrams of perfectly ordered and partially ordered spinels were obtained, which showed a clear correlation between the cation distribution and the reaction mechanisms.[27] One of the key findings suggests that the more ordered the material is, the less likely it is to access a solid solution region. On the other hand, increasing the Ni/Mn disorder in the Li-ion system stabilizes configurations at high Li contents, effectively enhancing the stability of solid solutions.[27] The enthalpy of formation results of this study suggest the same behavior in the case of the Na-ion system, in line with previous experimental demonstrations[10,11] as well as with the present prediction regarding phase transformation behavior. In addition, for the Li-ion system, a "uniform"[27] disordered distribution of Ni induces the largest solid solution reaction region, which is suggested to be achievable by controlled synthesis.[27]

Examining the $Na_{0.5}Mn_{1.5}Ni_{0.5}O_4$ lowest energy configurations of the P and F1−MNO structures reveals that Na-ions order in a Na-Va-Na-Va arrangement, the same as in the Li-ion case. The higher stability of the $Na_{0.5}Mn_{1.5}Ni_{0.5}O_4$ P configuration results in the small voltage step which is observed in Figure 6b. In Li-ion systems, this attribute is predicted and experimentally experienced in disordered spinels.[26] The difference between the two ions may be attributed to the larger structural penalties experienced by Na-ion insertion affecting the local preferable Na/Va−Mn/Ni arrangement. There is a probability that other disordered configurations (such as the uniform[27] disordered distribution) might lead to a more stable $Na_{0.5}Mn_{1.5}Ni_{0.5}O_4$ phase. Considering the experiments, this seems unlikely in the Na-ion case, given that no such voltage step is observed for either of the phases, as this effect is probably smoothened out in room temperature due to local disorder.[26]

Tuning of the termination of the phase separation region will lead to a better electrochemical performance, enabling the advantages (better cycling stability and kinetics) of solid solution insertion mechanisms.[10,11] Herein, the maximum solid solution region was determined with regard to the Ni clustered spinel. Considering the energy analysis in Section 3.1 and the relative stability results presented in Figure 7a, the clustered host is highly unlikely to occur. Because the Na system is found to behave extremely similar to the Li-ion system, it is expected that similar approaches[26,27] for improving the solid solution region are applicable. Similar to the Li system, here, we find that avoiding the ordered structure is of primary importance because it resists the most solid solution insertion.

3.3. Na-Ion Kinetics, Ni Migration, and Inverse Spinel Insights via MD simulations. To evaluate the kinetic properties of Na-ions in the spinel lattices, NEB and MD calculations were employed based on DFT. The spinel framework provides a diagonal 3D diffusion network for Na-ions connecting the tetrahedral (8a) positions via the metastable octahedral (16c) sites (Figure 9a).

For the Mn_2O_4 structure, the Na-ion migration path for the tetrahedral network was determined both at the high vacancy limit and at the dilute vacancy limit, using the NEB method (Figure 9b). We converged DFT + U NEB calculations, even though they are usually regarded difficult to converge due to the high metastability of the intermediate electronic states.[19] In line with earlier findings,[19,65,68] the similarity of the DFT + U and DFT results indicates that DFT + U does not necessarily lead to better results with regard to ion migration.

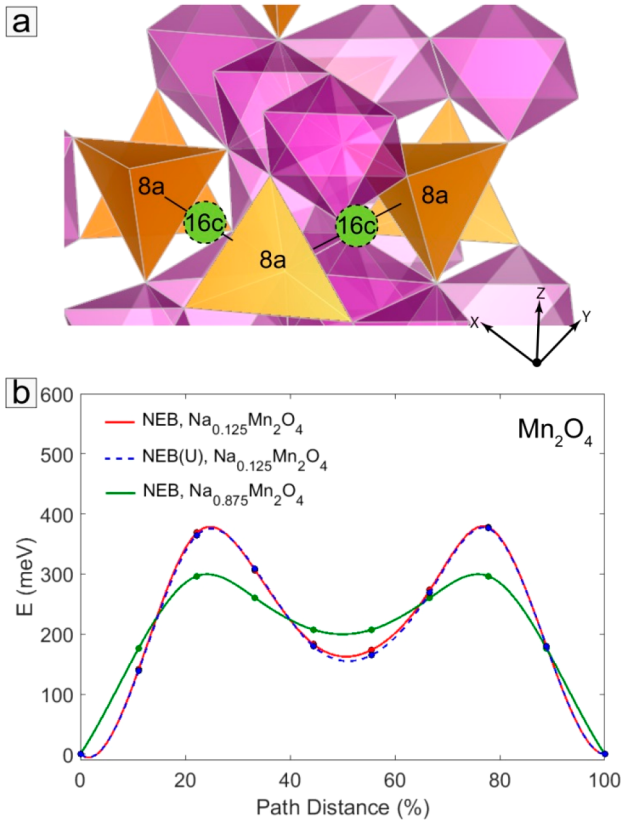

Figure 9. (a) Schematic representation of the 3D diffusion network in the spinel lattice. (b) Na-ion migration paths between the tetrahedral sites at the high vacancy limit (red solid and blue dashed lines) and at the dilute vacancy limit (green solid line) determined with NEB. The dashed blue line represents the DFT + U calculation.

In Figure 10, the predicted Na-ion migration path (purple color) is integrated on top of multivalent ion and Li-ion migration paths obtained from literature.[19] The divalent ions Zn^{2+} and Mg^{2+} display high barriers between 0.85 and 1.00 eV and 0.60 and 0.80 eV, respectively. Ca^{2+} (0.20−0.50 eV), on

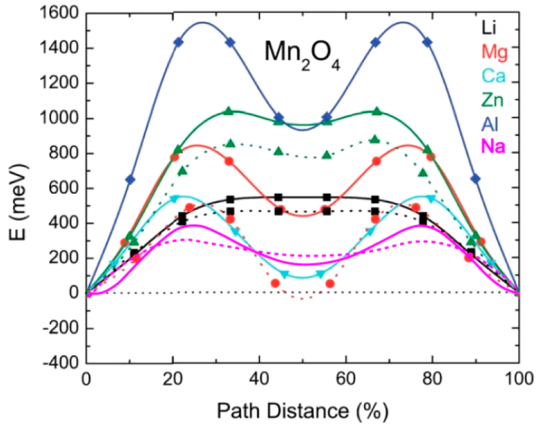

Figure 10. Migration barriers of multivalent ions and Li, reproduced from literature[19] published by The Royal Society of Chemistry. The lines for the Li, Mg, Ca, Zn, and Al represent the computed minimum energy paths for migration between the tetrahedral sites in the Mn_2O_4 spinel at the high vacancy limit (solid line) and dilute vacancy limit (dotted line), i.e. one mobile species per supercell.[19] The present Na-ion migration path (purple color) was added to the original figure.

DOI: 10.1021/acs.chemmater.8b01634
Chem. Mater. 2018, 30, 6646−6659

the other hand, demonstrates barriers close to Li^{1+} (0.40−0.60 eV). Finally, Na^{1+}, exhibiting energy barriers between 0.30 and 0.40 meV, outperforms the Zn^{2+}, Mg^{2+} multivalent carriers, having values comparable to those of Ca^{2+} and Li^{1+} despite its larger ionic radius. Low Na-ion energy barriers have also been reported for layered cathode and anode materials, as for instance, the O3 (0.20−0.28 eV) and P3 (0.20−0.48 eV) Na_xCrO_2 cathode material,[69] the P2 (0.12−0.19 meV) and P3 (0.22−0.25 eV) $NaTiO_2$ anode material,[70] and the O3 (0.125−0.28 eV) $NaTiO_2$ anode material.[52,71] Kinetic concerns rise in case of strong electrostatic repulsions between the Na ions that can occur either in structures that allow Na−Na close neighboring occupation (∼1.6 Å)[69] or by close interstitial Na−Na coexistence along the diffusion coordinate, blocking diffusion.[52] Generally, however, Na-ion kinetics look consistently facile in most materials, indicating that mobility is not a major concern, leaving cycling stability as the primary obstacle for SIBs implementation.

To further investigate the kinetic picture revealed by the NEB method, MD simulations were performed based on DFT. The Na-ion density plot for a 440 ps simulation of 1 Na-ion diffusing in the Mn_2O_4 unit cell lattice ($Na_{0.125}Mn_2O_4$) at 600 K is presented in Figure 11a. The Na-ion density indicates high Na mobility through the 8a-16c-8a sublattice, responsible for macroscopic diffusion, predicted within the MD time scales. The displacement of the atoms is presented in Supporting InformationA .

NEB convergence was not achieved for the MNO spinel structures due to large forces along the migration path. However, MD calculations provide insight regarding both stability and kinetics. An MD simulation for the F2−$Na_{0.125}Mn_{1.5}Ni_{0.5}O_4$ variant was performed at 600 K for 440 ps. The Na-ion density map of 1 diffusing Na-ion in the F2−MNO structure is presented in Figure 11b, and the atom displacements are presented in Supporting Information B. MD simulations predict that Ni atoms diffuse from the transition metal site into the 8a sites of the spinel structure. This occurs relatively fast (within ∼45 ps out of the total 440 ps). Mn atoms are migrating as well, albeit later, during the MD simulation (at approximately ∼89 ps out of the total 440). The structure appears to equilibrate after 100 ps (Figure 12), retaining the spinel framework. The Ni and Mn migration is a clear indication that the F2−$Na_{0.125}Mn_{1.5}Ni_{0.5}O_4$ configuration is transforming toward the inverse spinel structure at high temperatures. In total, 4 out of the 8 tetrahedral (and only partially the fifth) sites were occupied by Ni or Mn atoms, while the transition metal octahedral sites were occupied by vacancies, indicating that half of the material transformed to the inverse spinel configuration, whereas the other half remained in the normal spinel form (Figure 11b). Thereby, the MD simulations confirm that at elevated temperatures, many compounds with spinel lattices display both the normal and inverse cation arrangements, as experimentally observed.[62] The Na ion density (Figure 11b) is in the normal spinel configuration, where the Na-ion appears mobile. Ni and Mn are blocking the tetrahedral sites in the inverse spinel region, effectively prohibiting access to half of the unit cell, at least within the short time scale that can be simulated via MD. This demonstrates the superior kinetics of the normal spinels, confirming that a network of tetrahedral sites offers faster ion transport than a network of octahedral sites.[62,72] The dashed cyan circle in Figure 11b represents a tetrahedral 8a site that was partially occupied by Ni during the MD simulation, with

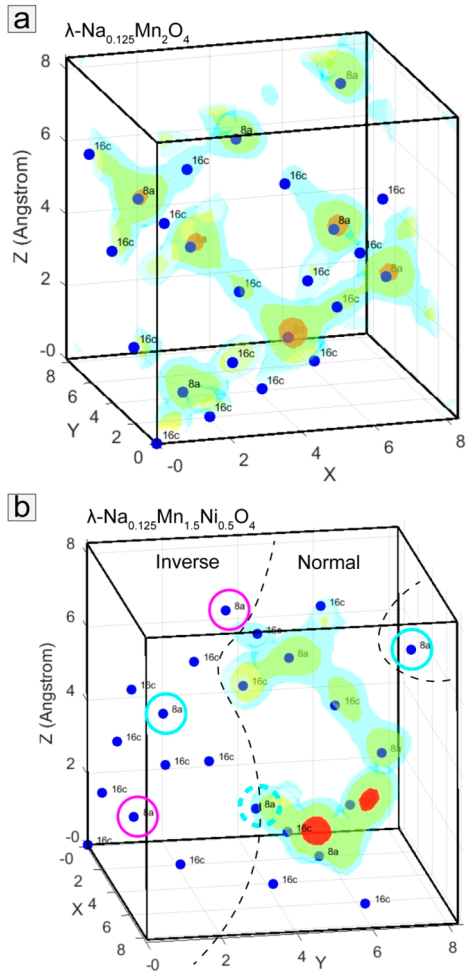

Figure 11. (a) Na-ion density during 440 ps MD simulation at 600 K for the $Na_{0.125}Mn_2O_4$ phase and (b) Na-ion density during 440 ps MD simulation at 600 K for the F2−$Na_{0.125}Mn_{1.5}Ni_{0.5}O_4$ phase. The blue and purple circles around the 8a positions indicate occupation by Ni and Mn, respectively, after the equilibration. The dashed circle indicates partial Ni occupation due to a sequence of back and forth hops (TM site to 8a, 8a to TM site, and TM to 8a).

Ni being able to hop back to its original transition metal octahedral site. It is also observed (Figure 11b), that when Na resides close to the normal/inverse boundary (dashed cyan circle) of the unit cell, it spends most of the time near a 16c octahedral environment. The Ni−O radial distribution function (RDF) for one of the nickel atoms before and after it moves to the new position is presented in Supporting Information B.

The same MD simulations were performed at 300 K to investigate possible Ni or Mn migration close to battery working temperatures. The structures were found to transform to the same equilibrium structure (displacements presented in Figure 13). In this case, however, only Ni relaxes to the tetrahedral site. During the MD simulations, Mn remains in its strongly distorted octahedral coordination, basically positioned between the tetrahedral-octahedral coordinations. The equilibrated (at room temperature) environment of the F2−$Na_{0.125}Mn_{1.5}Ni_{0.5}O_4$ spinel is presented in Figure 12.

With regard to F1 and P−$Na_{0.125}Mn_2O_4$ spinel structures, the MD simulations at 600 K reveal Ni migration into the tetrahedral sites, demonstrating that this phenomenon is independent of the Ni/Mn configuration. Contrary to the F2

DOI: 10.1021/acs.chemmater.8b01634
Chem. Mater. 2018, 30, 6646−6659

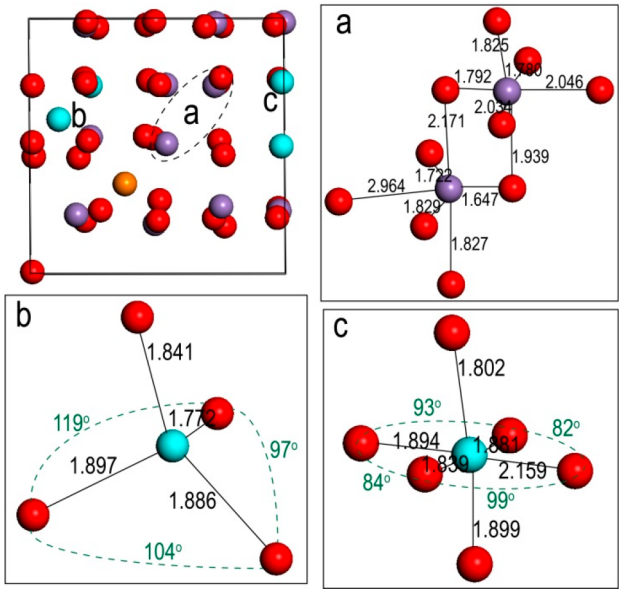

Figure 12. Snapshot of the equilibrated F2−$Na_{0.125}Mn_2O_4$ structure after 150 ps of the MD simulation at 300 K and local environments of (a) two Mn octahedral positions, one of the octahedral sites being very distorted, (b) the tetrahedral Ni coordination, and (c) the transition metal octahedral Ni coordination.

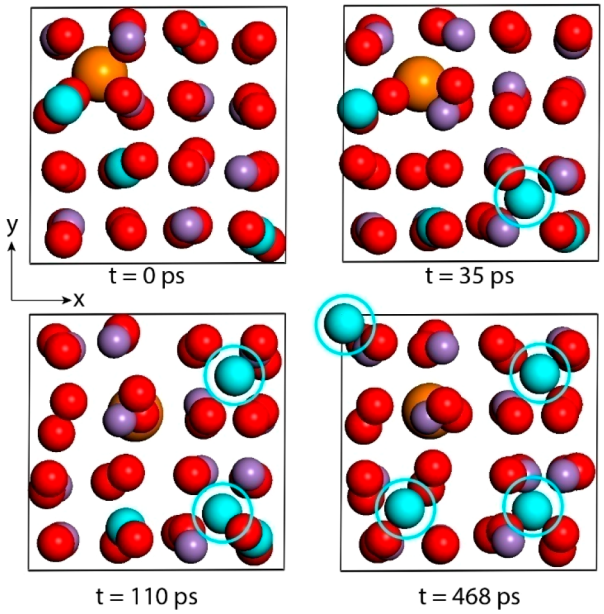

Figure 13. Snapshots of the P−$Na_{0.125}Mn_2O_4$ structure throughout the 500 ps MD simulation at 600 K: (top left) only Na occupies a tetrahedral position; (bottom right) all 4 Ni occupy tetrahedral positions.

spinel, no Mn migration was observed. The equilibration of the ordered P−$Na_{0.125}Mn_2O_4$ variant revealed that, within 500 ps, all 4 Ni atoms migrated and occupied tetrahedral positions, effectively blocking Na diffusion. Na mainly remained in its original position throughout the MD simulation. In addition, once two or more Ni occupy the tetrahedral positions, Na stabilizes in an octahedral environment for the rest of the simulation. Snapshots of the P−$Na_{0.125}Mn_2O_4$ structure throughout the MD simulation are presented in Figure 13. Atom displacements are presented in Supporting Information C.

Even though quantitative characterization of the MD results was not achieved, an interesting qualitative trend was discovered, where Ni (and even Mn) was shown to migrate into the tetrahedral sites, lowering the Na-ion diffusion. This migration leads to the inverse spinel structure and creates the conditions for interconversion between the various Ni/Mn configurations. Stability tests with the Bhattacharya and Wolverton method[62] for all Ni/Mn inverse spinel replacements is suggested to strengthen this argument. However, this is a subject for future work, beyond the length and focus of this study.

There is experimental evidence that Ni^{4+} migrates into the tetrahedral sites during Li extraction,[24,25] rationalizing the present predictions for its Na-ion counterpart. Experimentally, with regard to Ni doped variants, it has been observed that after the initial sodiation, there is a significant difficulty in extracting all the Na-ions out of the sodiated structure.[10,11] Ni migration, as revealed by MD simulations and/or partial conversion into the inverse structure, may rationalize this. The tetrahedral diffusion network at low Na concentrations is blocked, hindering Na movement and possibly trapping some part of the Na. In other words, when regions close to the surface are desodiated, the low Na concentration may lead to Ni migration toward tetrahedral sites, and/or partial formation of the inverse spinel, thus hindering full desodiation. Because we observed at least once Ni hopping back to its transition metal site within MD time scales, we speculate that resodiating the material may promote Ni to migrate back to its original octahedral position, potentially explaining why such kinetic difficulty is experienced only during desodiation.

4. CONCLUSIONS

Key thermodynamic and kinetic properties of Na-ion insertion in the λ-Mn_2O_4 and λ-$Mn_{1.5}Ni_{0.5}O_4$ spinels are revealed, adding to the understanding and facilitating improvement of the high voltage cathode materials for Na-ion batteries.

Full sodiation of the pure spinel was found to be thermodynamically possible. Two two-phase separation mechanisms are predicted, occurring at 3.2 and 2.4 V vs Na/Na^+, where Na is accommodated in the 8a and 16c interstitial positions, respectively. This is in agreement with experiments conducted in aqueous environment, showing reversible Na-ion insertion. All the spinel sodiated phases, however, are found to be metastable compared to O′3/O3 layered and postspinel structures. Lattice distortions upon Na (de)insertion may catalyze these phase transitions upon sodium cycling, rationalizing experimental findings of structural destabilization and partial phase transformation toward the O′3 layered lattice. The large lattice mismatch predicted for the endmember phases is expected to have an important effect in the cycling performance. Strain minimization should be prioritized to avoid material breakdown and/or phase transformations. Strain minimization could be achieved by nanosizing and fast cycling, suppressing the phase separation mechanism into solid solution Na-ion insertion (which is likely, considering the expected phase-coexistence energy penalty). This will improve the cycle life and moreover the kinetics as well as aid in avoiding the often sluggish diffusion over phase interfaces. Rapid Na-ion hopping is predicted by energy barrier calculations that are comparable to and lower than the ones predicted for Li-ion and multivalent ions, respectively. This

DOI: 10.1021/acs.chemmater.8b01634
Chem. Mater. 2018, 30, 6646−6659

was confirmed with MD simulations showing Na-ion diffusivity at short MD time scales. This means that once the structure destabilization and kinetic phase-interface limitations are overcome, good kinetic performance is expected, in agreement with experiments reporting an excellent rate capability.

With regard to the λ-$Mn_{1.5}Ni_{0.5}O_4$ spinel, we investigated several ordered/disordered phases, differing in the Ni distribution within the spinel lattice. The exact sodiation mechanism depends on the transition metal ordering, similar to the equivalent Li-ion structures. The Ni distribution greatly affects the relative stability of the intermediate phases and thus the reaction mechanisms. The ordered spinel is expected to sodiate via phase separation, exhibiting no solid solution. The disordered spinels, however, show stable intermediate phases in the $0.625 < x < 0.875$ ($Na_xMn_{1.5}Ni_{0.5}O_4$) concentration range, either by lowering the energy landscape due to a preferable Ni/Mn−Na/Va arrangement at this concentration range or by raising the energy of the fully sodiated endmember. Therefore, mixed reaction pathways of phase separation and solid solution reaction mechanisms are predicted in excellent agreement with experiments. This behavior is similar to that of the equivalent Li-ion structures. MD simulations revealed that Ni can diffuse from the TM site into the tetrahedral position (even at room temperature), which explains the kinetic limitations experienced experimentally during Na extraction. In addition, MD simulations point out that the λ-$Mn_{1.5}Ni_{0.5}O_4$ spinel converts into the inverse spinel under high temperatures, hindering Na-ion kinetics. MD results open up new possibilities in the study of inverse spinels and the effect on kinetic performance. Finally, Ni migration and partial transformation toward the inverted spinel may be considered phenomena of general interest, as they are also encountered in Li-ion batteries that show similar electrochemical behavior.

■ ASSOCIATED CONTENT

Supporting Information

The Supporting Information is available free of charge on the ACS Publications website at DOI: 10.1021/acs.chemmater.8b01634.

Atom displacements and radial distribution functions during molecular dynamics simulations (PDF)

■ AUTHOR INFORMATION

Corresponding Author

*E-mail: m.wagemaker@tudelft.nl.

ORCID

Niek J. J. de Klerk: 0000-0002-5100-4883

Marnix Wagemaker: 0000-0003-3851-1044

Notes

The authors declare no competing financial interest.

■ REFERENCES

(1) Mulder, F. M. Implications of diurnal and seasonal variations in renewable energy generation for large scale energy storage. *J. Renewable Sustainable Energy* **2014**, *6*, 033105.

(2) Palomares, V.; Casas-Cabanas, M.; Castillo-Martinez, E.; Han, M. H.; Rojo, T. Update on Na-based battery materials. A growing research path. *Energy Environ. Sci.* **2013**, *6*, 2312−2337.

(3) Kim, S. W.; Seo, D. H.; Ma, X. H.; Ceder, G.; Kang, K. Electrode Materials for Rechargeable Sodium-Ion Batteries: Potential Alternatives to Current Lithium-Ion Batteries. *Adv. Energy Mater.* **2012**, *2*, 710−721.

(4) Dai, Z. F.; Mani, U.; Tan, H. T.; Yan, Q. Y. Advanced Cathode Materials for Sodium-Ion Batteries: What Determines Our Choices? *Small Methods* **2017**, *1*, 1700098.

(5) Xiang, X. D.; Zhang, K.; Chen, J. Recent Advances and Prospects of Cathode Materials for Sodium-Ion Batteries. *Adv. Mater.* **2015**, *27*, 5343−5364.

(6) Kubota, K.; Komaba, S. Review-Practical Issues and Future Perspective for Na-Ion Batteries. *J. Electrochem. Soc.* **2015**, *162*, A2538−A2550.

(7) Kim, H.; Hong, J.; Park, K. Y.; Kim, H.; Kim, S. W.; Kang, K. Aqueous Rechargeable Li and Na Ion Batteries. *Chem. Rev.* **2014**, *114*, 11788−11827.

(8) Sawicki, M.; Shaw, L. L. Advances and challenges of sodium-ion batteries as post lithium ion batteries. *RSC Adv.* **2015**, *5*, 53129−53154.

(9) Luo, J. Y.; Cui, W. J.; He, P.; Xia, Y. Y. Raising the cycling stability of aqueous lithium-ion batteries by eliminating oxygen in the electrolyte. *Nat. Chem.* **2010**, *2*, 760−765.

(10) Kim, J. R.; Amatucci, G. G. Structural and Electrochemical Investigation of Na^+ Insertion into High-Voltage Spinel Electrodes. *Chem. Mater.* **2015**, *27*, 2546−2556.

(11) Kim, J. R.; Amatucci, G. G. $NaMn_{2-x}Ni_xO_4$ Derived from Mesoporous $LiMn_{2-x}Ni_xO_4$ High-Voltage Spinel Cathode Materials for Na-Ion Batteries. *J. Electrochem. Soc.* **2016**, *163*, A696−A705.

(12) Li, X.; Wu, D.; Zhou, Y. N.; Liu, L.; Yang, X. Q.; Ceder, G. O3-type $Na(Mn_{0.25}Fe_{0.25}Co_{0.25}Ni_{0.25})O_2$: A quaternary layered cathode compound for rechargeable Na ion batteries. *Electrochem. Commun.* **2014**, *49*, 51−54.

(13) Yuan, D. D.; Hu, X. H.; Qian, J. F.; Pei, F.; Wu, F. Y.; Mao, R. J.; Ai, X. P.; Yang, H. X.; Cao, Y. L. P2-type $Na_{0.67}Mn_{0.65}Fe_{0.2}Ni_{0.15}O_2$ Cathode Material with High-capacity for Sodium-ion Battery. *Electrochim. Acta* **2014**, *116*, 300−305.

(14) Tarascon, J. M.; Guyomard, D. G.; Wilkens, B.; Mckinnon, W. R.; Barboux, P. Chemical and Electrochemical Insertion of Na into the Spinel Lambda-MnO_2 Phase. *Solid State Ionics* **1992**, *57*, 113−120.

(15) Yabuuchi, N.; Yano, M.; Kuze, S.; Komaba, S. Electrochemical behavior and structural change of spinel-type $Li[Li_xMn_{2-x}]O_4$ (x = 0 and 0.2) in sodium cells. *Electrochim. Acta* **2012**, *82*, 296−301.

(16) Whitacre, J. F.; Wiley, T.; Shanbhag, S.; Wenzhuo, Y.; Mohamed, A.; Chun, S. E.; Weber, E.; Blackwood, D.; Lynch-Bell, E.; Gulakowski, J.; Smith, C.; Humphreys, D. An aqueous electrolyte, sodium ion functional, large format energy storage device for stationary applications. *J. Power Sources* **2012**, *213*, 255−264.

(17) Zhang, Y.; Yuan, C. L.; Ye, K.; Jiang, X.; Yin, J. L.; Wang, G. L.; Cao, D. X. An aqueous capacitor battery hybrid device based on Na-ion insertion-deinsertion in lambda-MnO_2 positive electrode. *Electrochim. Acta* **2014**, *148*, 237−243.

(18) Yuan, C. L.; Zhang, Y.; Pan, Y.; Liu, X. W.; Wang, G. L.; Cao, D. X. Investigation of the intercalation of polyvalent cations (Mg^{2+}, Zn^{2+}) into lambda-MnO_2 for rechargeable aqueous battery. *Electrochim. Acta* **2014**, *116*, 404−412.

(19) Liu, M.; Rong, Z. Q.; Malik, R.; Canepa, P.; Jain, A.; Ceder, G.; Persson, K. A. Spinel compounds as multivalent battery cathodes: a systematic evaluation based on ab initio calculations. *Energy Environ. Sci.* **2015**, *8*, 964−974.

(20) Cabana, J.; Casas-Cabanas, M.; Omenya, F. O.; Chernova, N. A.; Zeng, D. L.; Whittingham, M. S.; Grey, C. P. Composition-Structure Relationships in the Li-Ion Battery Electrode Material $LiNi_{0.5}Mn_{1.5}O_4$. *Chem. Mater.* **2012**, *24*, 2952−2964.

(21) Amdouni, N.; Zaghib, K.; Gendron, F.; Mauger, A.; Julien, C. M. Structure and insertion properties of disordered and ordered $LiNi_{0.5}Mn_{1.5}O_4$ spinels prepared by wet chemistry. *Ionics* **2006**, *12*, 117−126.

(22) Idemoto, Y.; Narai, H.; Koura, N. Crystal structure and cathode performance dependence on oxygen content of $LiMn_{1.5}Ni_{0.5}O_4$ as a cathode material for secondary lithium batteries. *J. Power Sources* **2003**, *119*, 125−129.

DOI: 10.1021/acs.chemmater.8b01634
Chem. Mater. 2018, 30, 6646−6659

(23) Pasero, D.; Reeves, N.; Pralong, V.; West, A. R. Oxygen nonstoichiometry and phase transitions in $LiMn_{1.5}Ni_{0.5}O_4$-delta. *J. Electrochem. Soc.* **2008**, *155*, A282−A291.
(24) Rana, J.; Glatthaar, S.; Gesswein, H.; Sharma, N.; Binder, J. R.; Chernikov, R.; Schumacher, G.; Banhart, J. Local structural changes in $LiMn_{1.5}Ni_{0.5}O_4$ spinel cathode material for lithium-ion batteries. *J. Power Sources* **2014**, *255*, 439−449.
(25) Kim, J. H.; Myung, S. T.; Yoon, C. S.; Kang, S. G.; Sun, Y. K. Comparative study of $LiNi_{0.5}Mn_{1.5}O_4$-delta and $LiNi_{0.5}Mn_{1.5}O_4$ cathodes having two crystallographic structures: $Fd\bar{3}m$ and $P4_332$. *Chem. Mater.* **2004**, *16*, 906−914.
(26) Lee, E.; Persson, K. A. Revealing the coupled cation interactions behind the electrochemical profile of $Li_xNi_{0.5}Mn_{1.5}O_4$. *Energy Environ. Sci.* **2012**, *5*, 6047−6051.
(27) Lee, E.; Persson, K. A. Solid-Solution Li Intercalation as a Function of Cation Order/Disorder in the High-Voltage $Li_xNi_{0.5}Mn_{1.5}O_4$ Spinel. *Chem. Mater.* **2013**, *25*, 2885−2889.
(28) Kresse, G.; Furthmuller, J. Efficiency of ab-initio total energy calculations for metals and semiconductors using a plane-wave basis set. *Comput. Mater. Sci.* **1996**, *6*, 15−50.
(29) Perdew, J. P.; Burke, K.; Ernzerhof, M. Generalized gradient approximation made simple. *Phys. Rev. Lett.* **1996**, *77*, 3865−3868.
(30) Lee, S. H.; Kang, J. H.; Kang, M. H. Structural properties of semiconductors in the generalized gradient approximation. *J. Korean Phys. Soc.* **1997**, *31*, 811−814.
(31) Blochl, P. E. Projector Augmented-Wave Method. *Phys. Rev. B: Condens. Matter Mater. Phys.* **1994**, *50*, 17953−17979.
(32) Anisimov, V. I.; Zaanen, J.; Andersen, O. K. Band Theory and Mott Insulators - Hubbard-U Instead of Stoner-I. *Phys. Rev. B: Condens. Matter Mater. Phys.* **1991**, *44*, 943−954.
(33) Anisimov, V. I.; Solovyev, I. V.; Korotin, M. A.; Czyzyk, M. T.; Sawatzky, G. A. Density-Functional Theory and Nio Photoemission Spectra. *Phys. Rev. B: Condens. Matter Mater. Phys.* **1993**, *48*, 16929−16934.
(34) Jain, A.; Hautier, G.; Ong, S. P.; Moore, C. J.; Fischer, C. C.; Persson, K. A.; Ceder, G. Formation enthalpies by mixing GGA and GGA plus U calculations. *Phys. Rev. B: Condens. Matter Mater. Phys.* **2011**, *84*, 045115.
(35) Wang, L.; Maxisch, T.; Ceder, G. Oxidation energies of transition metal oxides within the GGA+U framework. *Phys. Rev. B: Condens. Matter Mater. Phys.* **2006**, *73*, 195107.
(36) Kim, H.; Kim, D. J.; Seo, D. H.; Yeom, M. S.; Kang, K.; Kim, D. K.; Jung, Y. Ab Initio Study of the Sodium Intercalation and Intermediate Phases in $Na_{0.44}MnO_2$ for Sodium-Ion Battery. *Chem. Mater.* **2012**, *24*, 1205−1211.
(37) Greedan, J. E.; Raju, N. P.; Wills, A. S.; Morin, C.; Shaw, S. M.; Reimers, J. N. Structure and magnetism in lambda-MnO_2. Geometric frustration in a defect spinel. *Chem. Mater.* **1998**, *10*, 3058−3067.
(38) Noda, Y.; Ohno, K.; Nakamura, S. Momentum-dependent band spin splitting in semiconducting MnO_2: a density functional calculation. *Phys. Chem. Chem. Phys.* **2016**, *18*, 13294−13303.
(39) Biskup, N.; Martinez, J. L.; de Dompablo, M. E. A. Y.; Diaz-Carrasco, P.; Morales, J. Relation between the magnetic properties and the crystal and electronic structures of manganese spinels $LiNi_{0.5}Mn_{1.5}O_4$ and $LiCu_{0.5}Mn_{1.5}O_{4-\delta}$ ($0 < \delta < 0.125$). *J. Appl. Phys.* **2006**, *100*, 093908.
(40) Kitchaev, D. A.; Peng, H. W.; Liu, Y.; Sun, J. W.; Perdew, J. P.; Ceder, G. Energetics of MnO_2 polymorphs in density functional theory. *Phys. Rev. B: Condens. Matter Mater. Phys.* **2016**, *93*, 045132.
(41) Van der Ven, A.; Aydinol, M. K.; Ceder, G.; Kresse, G.; Hafner, J. First-principles investigation of phase stability in $LixCoO_2$. *Phys. Rev. B: Condens. Matter Mater. Phys.* **1998**, *58*, 2975−2987.
(42) Wagemaker, M.; Van Der Ven, A.; Morgan, D.; Ceder, G.; Mulder, F. M.; Kearley, G. J. Thermodynamics of spinel Li_xTiO_2 from first principles. *Chem. Phys.* **2005**, *317*, 130−136.
(43) Aydinol, M. K.; Kohan, A. F.; Ceder, G.; Cho, K.; Joannopoulos, J. Ab initio study of lithium intercalation in metal oxides and metal dichalcogenides. *Phys. Rev. B: Condens. Matter Mater. Phys.* **1997**, *56*, 1354−1365.
(44) Islam, M. S.; Fisher, C. A. J. Lithium and sodium battery cathode materials: computational insights into voltage, diffusion and nanostructural properties. *Chem. Soc. Rev.* **2014**, *43*, 185−204.
(45) de Klerk, N. J. J.; Wagemaker, M. Analysis of Diffusion in Solid-State Electrolytes through MD Simulations, Improvement of the Li-Ion Conductivity in β-Li_3PS_4 as an Example. *ACS Appl. Energy Mater.* **2018**, *1*, 3230−3242.
(46) Xia, H.; Meng, Y. S.; Lu, L.; Ceder, G. Electrochemical properties of nonstoichiometric $LiNi_{0.5}Mn_{1.5}O_{4-\delta}$ thin-film electrodes prepared by pulsed laser deposition. *J. Electrochem. Soc.* **2007**, *154*, A737−A743.
(47) Vadlamani, B.; An, K.; Jagannathan, M.; Chandran, K. S. R. An In-Situ Electrochemical Cell for Neutron Diffraction Studies of Phase Transitions in Small Volume Electrodes of Li-Ion Batteries. *J. Electrochem. Soc.* **2014**, *161*, A1731−A1741.
(48) Kitchaev, D. A.; Dacek, S. T.; Sun, W. H.; Ceder, G. Thermodynamics of Phase Selection in MnO_2 Framework Structures through Alkali Intercalation and Hydration. *J. Am. Chem. Soc.* **2017**, *139*, 2672−2681.
(49) Tompsett, D. A.; Islam, M. S. Electrochemistry of Hollandite alpha-MnO2: Li-Ion and Na-Ion Insertion and Li_2O Incorporation. *Chem. Mater.* **2013**, *25*, 2515−2526.
(50) Karim, A.; Fosse, S.; Persson, K. A. Surface structure and equilibrium particle shape of the $LiMn_2O_4$ spinel from first-principles calculations. *Phys. Rev. B: Condens. Matter Mater. Phys.* **2013**, *87*, 075322.
(51) Ning, F. H.; Xu, B.; Shi, J.; Su, H. B.; Wu, M. S.; Liu, G.; Ouyang, C. Y. Ab initio investigation of Jahn-Teller-distortion-tuned Li-ion migration in lambda-MnO_2. *J. Mater. Chem. A* **2017**, *5*, 9618−9626.
(52) Vasileiadis, A.; Wagemaker, M. Thermodynamics and Kinetics of Na-Ion Insertion into Hollandite-TiO_2 and O3-Layered $NaTiO_2$: An Unexpected Link between Two Promising Anode Materials for Na-Ion Batteries. *Chem. Mater.* **2017**, *29*, 1076−1088.
(53) Ling, C.; Mizuno, F. Phase Stability of Post-spinel Compound AMn_2O_4 (A = Li, Na, or Mg) and Its Application as a Rechargeable Battery Cathode. *Chem. Mater.* **2013**, *25*, 3062−3071.
(54) Ma, X. H.; Chen, H. L.; Ceder, G. Electrochemical Properties of Monoclinic $NaMnO_2$. *J. Electrochem. Soc.* **2011**, *158*, A1307−A1312.
(55) de Klerk, N. J. J.; Vasileiadis, A.; Smith, R. B.; Bazant, M. Z.; Wagemaker, M. Explaining key propperties of lithiation in TiO_2-anatase Li-ion battery electrodes using phase field modeling. *Phys. Rev. Mater.* **2017**, *1*, 025404.
(56) Bazant, M. Z. Theory of Chemical Kinetics and Charge Transfer based on Nonequilibrium Thermodynamics. *Acc. Chem. Res.* **2013**, *46*, 1144−1160.
(57) Bai, P.; Cogswell, D. A.; Bazant, M. Z. Suppression of Phase Separation in LiFePO+ Nanoparticles During Battery Discharge. *Nano Lett.* **2011**, *11*, 4890−4896.
(58) Zhang, X. Y.; van Hulzen, M.; Singh, D. P.; Brownrigg, A.; Wright, J. P.; van Dijk, N. H.; Wagemaker, M. Direct view on the phase evolution in individual $LiFePO_4$ nanoparticles during Li-ion battery cycling. *Nat. Commun.* **2015**, *6*, 8333.
(59) Zhang, X. Y.; van Hulzen, M.; Singh, D. P.; Brownrigg, A.; Wright, J. P.; van Dijk, N. H.; Wagemaker, M. Rate-Induced Solubility and Suppression of the First-Order Phase Transition in Olivine $LiFePO_4$. *Nano Lett.* **2014**, *14*, 2279−2285.
(60) Niu, J. J.; Kushima, A.; Qian, X. F.; Qi, L.; Xiang, K.; Chiang, Y. M.; Li, J. In Situ Observation of Random Solid Solution Zone in $LiFePO_4$ Electrode. *Nano Lett.* **2014**, *14*, 4005−4010.
(61) Akimoto, J.; Awaka, J.; Kijima, N.; Takahashi, Y.; Maruta, Y.; Tokiwa, K.; Watanabe, T. High-pressure synthesis and crystal structure analysis of $NaMn_2O_4$ with the calcium ferrite-type structure. *J. Solid State Chem.* **2006**, *179*, 169−174.
(62) Bhattacharya, J.; Wolverton, C. Relative stability of normal vs. inverse spinel for 3d transition metal oxides as lithium intercalation cathodes. *Phys. Chem. Chem. Phys.* **2013**, *15*, 6486−6498.

DOI: 10.1021/acs.chemmater.8b01634
Chem. Mater. 2018, 30, 6646−6659

(63) Bhattacharya, J.; Van der Ven, A. Phase stability and nondilute Li diffusion in spinel $Li_{1+x}Ti_2O_4$. *Phys. Rev. B: Condens. Matter Mater. Phys.* **2010**, *81*, 104304.
(64) Ouyang, C. Y.; Shi, S. Q.; Lei, M. S. Jahn-Teller distortion and electronic structure of $LiMn_2O_4$. *J. Alloys Compd.* **2009**, *474*, 370−374.
(65) Xu, B.; Meng, S. Factors affecting Li mobility in spinel $LiMn_2O_{4-\alpha}$ first-principles study by GGA and GGA plus U methods. *J. Power Sources* **2010**, *195*, 4971−4976.
(66) Radin, M. D.; Van der Ven, A. Simulating Charge, Spin, and Orbital Ordering: Application to Jahn-Teller Distortions in Layered Transition-Metal Oxides. *Chem. Mater.* **2018**, *30*, 607−618.
(67) Ohzuku, T.; Kitagawa, M.; Hirai, T. Electrochemistry of Manganese-Dioxide in Lithium Nonaqueous Cell 0.3. X-Ray Diffractional Study on the Reduction of Spinel-Related Manganese-Dioxide. *J. Electrochem. Soc.* **1990**, *137*, 769−775.
(68) Dathar, G. K. P.; Sheppard, D.; Stevenson, K. J.; Henkelman, G. Calculations of Li-Ion Diffusion in Olivine Phosphates. *Chem. Mater.* **2011**, *23*, 4032−4037.
(69) Mo, Y. F.; Ong, S. P.; Ceder, G. Insights into Diffusion Mechanisms in P_2 Layered Oxide Materials by First-Principles Calculations. *Chem. Mater.* **2014**, *26*, 5208−5214.
(70) Guo, S. H.; Sun, Y.; Yi, J.; Zhu, K.; Liu, P.; Zhu, Y. B.; Zhu, G. Z.; Chen, M. W.; Ishida, M.; Zhou, H. S. Understanding sodium-ion diffusion in layered P2 and P3 oxides via experiments and first-principles calculations: a bridge between crystal structure and electrochemical performance. *NPG Asia Mater.* **2016**, *8*, e266.
(71) Wu, D.; Li, X.; Xu, B.; Twu, N.; Liu, L.; Ceder, G. $NaTiO_2$: a layered anode material for sodium-ion batteries. *Energy Environ. Sci.* **2015**, *8*, 195−202.
(72) Bhattacharya, J.; Van der Ven, A. First-principles study of competing mechanisms of nondilute Li diffusion in spinel Li_xTiS_2. *Phys. Rev. B: Condens. Matter Mater. Phys.* **2011**, *83*, 144302.

DOI: 10.1021/acs.chemmater.8b01634
Chem. Mater. 2018, 30, 6646−6659